

# TC-LIF: A Two-Compartment Spiking Neuron Model for Long-term Sequential Modelling

Shimin Zhang<sup>1\*</sup>, Qu Yang<sup>2\*</sup>, Chenxiang Ma<sup>1</sup>, Jibin Wu<sup>1†</sup>, Haizhou Li<sup>2,3</sup>, Kay Chen Tan<sup>1</sup>

<sup>1</sup>The Hong Kong Polytechnic University

<sup>2</sup>National University of Singapore

<sup>3</sup>The Chinese University of Hong Kong, Shenzhen, China

## Abstract

The identification of sensory cues associated with potential opportunities and dangers is frequently complicated by unrelated events that separate useful cues by long delays. As a result, it remains a challenging task for state-of-the-art spiking neural networks (SNNs) to establish long-term temporal dependency between distant cues. To address this challenge, we propose a novel biologically inspired Two-Compartment Leaky Integrate-and-Fire spiking neuron model, dubbed TC-LIF. The proposed model incorporates carefully designed somatic and dendritic compartments that are tailored to facilitate learning long-term temporal dependencies. Furthermore, a theoretical analysis is provided to validate the effectiveness of TC-LIF in propagating error gradients over an extended temporal duration. Our experimental results, on a diverse range of temporal classification tasks, demonstrate superior temporal classification capability, rapid training convergence, and high energy efficiency of the proposed TC-LIF model. Therefore, this work opens up a myriad of opportunities for solving challenging temporal processing tasks on emerging neuromorphic computing systems.

## Introduction

Spiking neural networks (SNNs) have attracted significant attention recently owing to their biological plausibility and potential for energy-efficient neural computation (Maass 1997; Pfeiffer and Pfeil 2018). The fundamental computing units of SNNs, known as spiking neurons, aim to emulate the rich neuronal dynamics observed in biological neurons, which facilitate the encoding, processing, and storage of spatio-temporal patterns (Gerstner et al. 2014). Furthermore, spiking neurons communicate with each other via discrete spikes, such event-driven operation leads to ultra-low-power neural computation (Davies et al. 2018; Pei et al. 2019).

In practice, single-compartment spiking neurons models have been widely adopted for large-scale brain simulations and neuromorphic computing, instances include Leaky Integrate-and-Fire (LIF) Model (Abbott and Kepler 2005), Izhikevich Model (Izhikevich 2003), and Adaptive Exponential Integrate-and-Fire (AdEx) Model (Brette and Gerstner 2005). These single-compartment models abstract the biological neuron as a single electrical circuit, preserving

the essential neuronal dynamics of biological neurons while ignoring the complex geometrical structure of dendrites as well as their interactions with the soma. This degree of abstraction significantly reduces the modeling effort, making them more feasible to study the behavior of large-scale biological neural networks and perform complex pattern recognition tasks on neuromorphic computing systems.

While single-compartment spiking neuron models have demonstrated promising results on pattern recognition tasks with limited temporal context (Tavanaei et al. 2019; Zhang et al. 2021; Wu et al. 2021; Bu et al. 2023; Yang et al. 2022; Yao et al. 2022), their ability to solve tasks that require long-term temporal dependencies remains constrained. This issue primarily arises from the difficulty of performing long-term temporal credit assignment (TCA) in SNNs. The TCA involves the identification of input spikes that contribute to future rewards or penalties, and subsequently strengthen or weaken their respective connections. Given the discrete and sequential nature of spikes, pinpointing the exact moments or sequences that led to a prediction error becomes challenging. This issue deteriorates for long sequences, where the influence of early spikes on later predictions is more challenging to trace. Hence, addressing the TCA problem is crucial for enhancing the sequential modeling capabilities of SNNs.

Broadly speaking, there are two research directions have been pursued to address the TCA problem in SNNs. The first direction draws inspiration from the recent success of attention models within deep learning. These methods integrate the self-attention mechanism into SNNs to enable the direct modeling of temporal relationships between different time steps (Qin et al. 2023; Yao et al. 2021). However, the self-attention mechanism is computationally expensive to operate, and it is unable to operate in real-time. Furthermore, self-attention is not directly compatible with mainstream neuromorphic chips, therefore, it cannot take advantage of the energy efficiency offered by these chips.

The latter research direction primarily centers around the idea of adaptive spiking neuron models. Notable efforts include the Long Short-Term Memory Spiking Neural Network (LSNN) (Bellec et al. 2018). LSNN introduces an adaptive firing threshold mechanism into LIF neurons, whereby the neuronal firing threshold increases following each firing event and slowly decays back to the resting-state firing threshold. This elevation in the firing threshold serves

\*Equal contribution

†Corresponding Author: jibin.wu@polyu.edu.hk

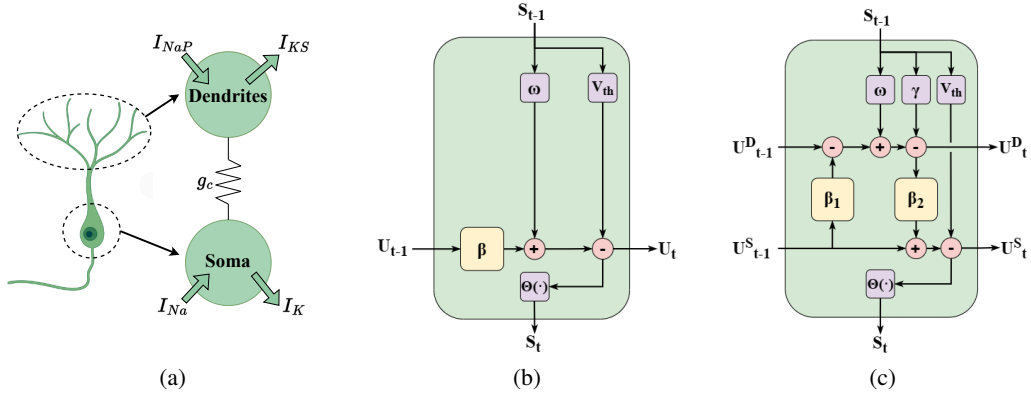


Figure 1: Illustration of (a) the structure of a two-compartment Prinsky-Rinzel pyramidal neuron, and the internal operations of (b) LIF model as well as the proposed (c) TC-LIF model.

as a means of information storage, particularly when combined with a slow decay rate, effectively facilitating long-term TCA (Bellec et al. 2020). Additional studies have proposed the utilization of learnable time constants (Yin, Corradi, and Bohté 2020, 2021) or dual time constants (Shaban, Bezugam, and Suri 2021) for the adaptive firing threshold, such that multi-scale temporal information can be retained and leveraged to perform TCA. However, these studies have predominantly focused on enhancing the neuronal firing threshold, which, as a simple neuronal component, possesses inherent restrictions in terms of information storage capacity. Consequently, these models face inherent limitations in their capabilities to address the TCA problem.

Multi-compartment spiking neuron models have been the subject of extensive research in the field of neuroscience (Rall 1964; Pinsky and Rinzel 1994). These models aim to faithfully model the complex geometric structure of dendrites, along with the interactions between dendritic and somatic compartments. As a result, multi-compartment models provide a more accurate representation of the complex neuronal dynamics observed in biological neurons, facilitating information interaction across various temporal scales (Stuart and Spruston 2015). Consequently, they present a promising avenue for addressing the challenge of long-term TCA. While incorporating more compartments offers additional benefits of expanded memory capacity, the increased model complexity may hinder their practical use, especially for solving complex pattern recognition tasks.

In this paper, we derive a generalized two-compartment neuron model as depicted in Figure 1(a). This neuron model provides an ideal reflection of the minimal geometry of the well-known Prinsky-Rinzel (P-R) pyramidal neuron while preserving the essential features of more complicated multi-compartment models (Lin et al. 2017). Based on this, we further proposed a two-compartment spiking neuron model, called TC-LIF (Two-Compartment Leaky Integrate-and-Fire), which is tailored to address the long-term TCA problem. The main contributions of our work are summarized as follows:

- We propose a brain-inspired two-compartment spiking

neuron model, dubbed TC-LIF, which has been carefully designed to facilitate long-term sequential modeling.

- We provide theoretical and experimental analysis to validate the effectiveness of the proposed TC-LIF model in achieving successful long-term TCA.
- Our experimental results, on a broad range of temporal classification tasks, demonstrate superior sequential modeling capabilities of TC-LIF over single-compartment neuron models, including enhanced classification accuracy, rapid training convergence, and high energy efficiency.

## Methodology

In this section, we first introduce a conventional single-compartment neuron model, specifically the LIF model. We delve into its inherent limitation in effectively learning long-term dependencies. Then, we present a generalized two-compartment spiking neuron model inspired by the well-known Prinsky-Rinzel pyramidal neurons (Pinsky and Rinzel 1994). This set the stage for the development of our proposed TC-LIF model, meticulously tailored to address the long-term TCA problem. Furthermore, we provide a theoretical analysis to elucidate the mechanisms through which the TC-LIF model effectively facilitates long-term TCA.

### LIF Neurons Struggle to Perform Long-term TCA

In general, spiking neurons integrate synaptic inputs, transduced from the incoming spikes, into their membrane potentials. Once the accumulated membrane potential surpasses the firing threshold, an output spike will be generated and transmitted to subsequent neurons. The LIF neuron is the most ubiquitous and effective single-compartment spiking neuron model, which has been widely used for large-scale brain simulation and neuromorphic computing. The neuronal dynamics of a LIF neuron can be described by the fol-

lowing discrete-time formulations:

$$\mathcal{U}[t] = \beta \mathcal{U}[t-1] - \mathcal{V}_{th} \mathcal{S}[t-1] + \mathcal{I}[t] \quad (1)$$

$$\mathcal{I}[t] = \sum_i \omega_i \mathcal{S}_i[t-1] + b \quad (2)$$

$$\mathcal{S}[t] = \Theta(\mathcal{U}[t] - \mathcal{V}_{th}) \quad (3)$$

where  $\mathcal{U}[t]$  and  $\mathcal{I}[t]$  represent the membrane potential and the input current of a neuron at time  $t$ , respectively. The term  $\beta \equiv \exp(-dt/\tau_m)$  is the membrane decaying coefficient that ranged from (0, 1), in which  $\tau_m$  is the membrane time constant and  $dt$  is the simulation time step.  $\omega_i$  denotes the synaptic weight that connects input neuron  $i$ , and  $b$  represents the bias term. An output spike will be generated once the membrane potential  $\mathcal{U}[t]$  reaches the neuronal firing threshold  $\mathcal{V}_{th}$  as per Eq. (3).

The backpropagation-through-time (BPTT) algorithm, coupled with surrogate gradients, has been recently proposed as an effective approach to perform credit assignment in SNNs (Wu et al. 2018; Neftci, Mostafa, and Zenke 2019). While this approach demonstrates effectiveness in tasks that involve limited temporal context, it encounters limitations when confronted with tasks that necessitate long-term temporal dependencies. This is primarily attributed to the vanishing gradient problem, where the error gradients diminish during the backpropagation process. To further elaborate on this issue, let us consider the training of a SNN with the following objective function:

$$\mathcal{L}(\hat{\mathcal{S}}, \mathcal{S}) = \frac{1}{N} \sum_{n=1}^N \mathcal{L}(\hat{\mathcal{S}}_n, \mathcal{S}_n) \quad (4)$$

where  $N$  is the number of training samples,  $\mathcal{L}$  is the loss function,  $\mathcal{S}_n$  is the network output, and  $\hat{\mathcal{S}}_n$  is the training target. Following the BPTT algorithm, the gradient with respect to the weight  $\omega$  can be calculated as follows:

$$\frac{\partial \mathcal{L}}{\partial \omega} = \sum_{t=1}^T \frac{\partial \mathcal{L}}{\partial \mathcal{S}[T]} \frac{\partial \mathcal{S}[T]}{\partial \mathcal{U}[T]} \frac{\partial \mathcal{U}[T]}{\partial \mathcal{U}[t]} \frac{\partial \mathcal{U}[t]}{\partial \omega} \quad (5)$$

where for a LIF neuron with the membrane decaying rate of  $\beta \in (0, 1)$ :

$$\frac{\partial \mathcal{U}[T]}{\partial \mathcal{U}[t]} = \prod_{i=t+1}^T \frac{\partial \mathcal{U}[i]}{\partial \mathcal{U}[i-1]} = \beta^{(T-t)} \quad (6)$$

It is obvious that as the time step  $T$  increases, the impact of time step  $t$  on its subsequent time step diminishes. This is because the membrane potential decay causes an exponential decay of early information. This problem becomes exacerbated when  $t$  is considerably smaller than  $T$ , and the value of Eq. (6) tends to 0, thus leading to the vanishing gradient problem. Consequently, the existing single-compartment neuron models, such as the LIF model, face challenges in effectively propagating gradients to significantly earlier time steps. This poses a significant limitation in learning long-term dependencies, which motivates us to develop two-compartment neuron models that possess enhanced capabilities in facilitating long-term TCA.

## A Generalized Two-Compartment Spiking Neuron

The P-R pyramidal neurons are located in the CA3 region of the hippocampus, which plays an important role in memory storage and retrieval of animals (Pinsky and Rinzel 1994). Researchers have simplified this neuron model as a two-compartment model that can simulate the interaction between somatic and dendritic compartments, as depicted in Figure 1(a). Drawing upon the structure of the P-R model, we develop a generalized two-compartment spiking neuron model that defined as the following. The detailed derivations of this formulation are provided in Supplementary Materials.

$$\mathcal{U}^D[t] = \alpha_1 \mathcal{U}^D[t-1] + \beta_1 \mathcal{U}^S[t-1] + \mathcal{I}[t] \quad (7)$$

$$\mathcal{U}^S[t] = \alpha_2 \mathcal{U}^S[t-1] + \beta_2 \mathcal{U}^D[t] - \mathcal{V}_{th} \mathcal{S}[t-1] \quad (8)$$

$$\mathcal{S}[t] = \Theta(\mathcal{U}^S[t] - \mathcal{V}_{th}) \quad (9)$$

where  $\mathcal{U}^D$  and  $\mathcal{U}^S$  represents the membrane potentials of the dendritic and the somatic compartments, respectively.  $\alpha_1$  and  $\alpha_2$  are respective membrane potential decaying coefficients for these two compartments. Notably, the membrane potentials of these two compartments are not updated independently. Rather, they are coupled with each other through the second term in Eqs. (7) and (8), in which the coupling effects are controlled by the coefficients  $\beta_1$  and  $\beta_2$ . The interplay between these two compartments enhances the neuronal dynamics and, if properly designed, can resolve the vanishing gradient problem.

## TC-LIF Spiking Neuron Model

Based on the generalized two-compartment spiking neuron model derived earlier, we propose a TC-LIF neuron model that has been carefully designed to facilitate long-term sequential modeling. In comparison to the generalized two-compartment neuron model, we drop the membrane decaying factors  $\alpha_1$  and  $\alpha_2$  from both compartments. This modification aims to circumvent the rapid decay of memory that could cause unintended information loss. Moreover, to circumvent excess firing caused by persistent input accumulation, we set  $\beta_1$  and  $\beta_2$  to opposite signs. The dynamics of the proposed TC-LIF model are expressed as follows:

$$\mathcal{U}^D[t] = \mathcal{U}^D[t-1] + \beta_1 \mathcal{U}^S[t-1] + \mathcal{I}[t] - \gamma \mathcal{S}[t-1] \quad (10)$$

$$\mathcal{U}^S[t] = \mathcal{U}^S[t-1] + \beta_2 \mathcal{U}^D[t] - \mathcal{V}_{th} \mathcal{S}[t-1] \quad (11)$$

$$\mathcal{S}[t] = \Theta(\mathcal{U}^S[t] - \mathcal{V}_{th}) \quad (12)$$

where the coefficients  $\beta_1 \equiv -\sigma(c_1)$  and  $\beta_2 \equiv \sigma(c_2)$  determine the interaction between these two compartments. Here, the sigmoid function  $\sigma(\cdot)$  is utilized to ensure two coefficients are within the range of (-1, 0) and (0, 1), and the parameters  $c_1$  and  $c_2$  can be automatically adjusted during the training process. The effect of this design choice will be analyzed in detail soon. The membrane potentials of both compartments are reset after the firing of the soma. Notably, the reset of the dendritic compartment is triggered by the backpropagating spike that is governed by a scaling factor  $\gamma$ . The internal operations of the TC-LIF model are depicted

in Figure 1(c), which exhibits richer internal dynamics in comparison to the LIF model that is shown in Figure 1(b).

According to the above formulations,  $\mathcal{U}^S$  is responsible for retaining short-term memory of dendritic inputs, which will be reset after neuron firing. In contrast,  $\mathcal{U}^D$  serves as a long-term memory that retains the information about external inputs, which is only partially reset by the backpropagating spike from the soma. In this way, the multi-scale temporal information is effectively preserved in TC-LIF. To further demonstrate the superiority of TC-LIF in facilitating long-term TCA, we provide a theoretical analysis below to demonstrate why the TC-LIF model can greatly alleviate the vanishing gradient problem.

As discussed earlier, the primary cause of the gradient vanishing problem is attributed to the recursive computation of  $\partial\mathcal{U}[T]/\partial\mathcal{U}[t]$ . This problem can, however, be effectively alleviated in the proposed TC-LIF model, whose partial derivative  $\partial\mathcal{U}[T]/\partial\mathcal{U}[t]$  can be calculated as follows:

$$\frac{\partial\mathcal{U}[T]}{\partial\mathcal{U}[t]} = \prod_{j=t+1}^T \frac{\partial\mathcal{U}[j]}{\partial\mathcal{U}[j-1]}, \quad \mathcal{U}[j] = [\mathcal{U}^D[j], \mathcal{U}^S[j]]^T \quad (13)$$

where

$$\begin{aligned} \frac{\partial\mathcal{U}[j]}{\partial\mathcal{U}[j-1]} &= \begin{bmatrix} \frac{\partial\mathcal{U}^D[j]}{\partial\mathcal{U}^D[j-1]} & \frac{\partial\mathcal{U}^D[j]}{\partial\mathcal{U}^S[j-1]} \\ \frac{\partial\mathcal{U}^S[j]}{\partial\mathcal{U}^D[j-1]} & \frac{\partial\mathcal{U}^S[j]}{\partial\mathcal{U}^S[j-1]} \end{bmatrix} \\ &= \begin{bmatrix} \beta_1\beta_2 + 1 & \beta_1 \\ \beta_1\beta_2^2 + 2\beta_2 & \beta_1\beta_2 + 1 \end{bmatrix} \end{aligned} \quad (14)$$

In order to quantify the severity of the vanishing gradient problem in TC-LIF, we further calculate the column infinite norm as provided in Eq. (15) below.

$$\begin{aligned} \left\| \frac{\partial\mathcal{U}[j]}{\partial\mathcal{U}[j-1]} \right\|_{\infty} &= \max(\beta_1\beta_2^2 + \beta_1\beta_2 + 2\beta_2 + 1, \\ &\quad \beta_1\beta_2 + \beta_1 + 1) \\ &= \beta_1\beta_2^2 + \beta_1\beta_2 + 2\beta_2 + 1 \end{aligned} \quad (15)$$

The infinite norm signifies the maximum changing rate of membrane potentials over a prolonged time period. By employing the constrained optimization method to solve the lower bound of the infinite norm for  $\|\partial\mathcal{U}[j]/\partial\mathcal{U}[j-1]\|_{\infty}$ , it can be found that this value is larger than 1. This suggests that the TC-LIF model can effectively address the vanishing gradient problem. Nevertheless, given that  $\beta$  consistently exceeds 1, it inevitably faces the gradient exploding problem. Fortunately, our experimental studies show that this value is marginally greater than 1 for the majority of  $\{\beta_1, \beta_2\}$  selected from the second quadrant, thereby leading to stable training. See more analysis in Supplementary Materials.

It is worth noting that the TC-LIF model can be reformulated into a single-compartment form:

$$\begin{aligned} \mathcal{U}^S[t] &= (1 + \beta_1\beta_2)\mathcal{U}^S[t-1] + \beta_2\mathcal{U}^D[t-1] + \\ &\quad \beta_2\mathcal{I}[t] - (\beta_2\gamma + \mathcal{V}_{th})\mathcal{S}[t-1] \end{aligned} \quad (16)$$

In essence, the above formulation mirrors a LIF neuron that is characterized by a decaying input. As a result, the proposed model is appropriately referred to as TC-LIF. Although the memory decaying problem persists in the TC-LIF model, the presence of  $\mathcal{U}^D$  can effectively compensate for the memory loss and address the vanishing gradient problem.

## Experiments

In this section, we first explore the parameter space for the generalized two-compartment neurons to validate the design of TC-LIF. Then, we evaluate the TC-LIF model on various temporal classification benchmarks, including sequential MNIST (S-MNIST), permuted sequential MNIST (PS-MNIST), Google Speech Commands (GSC), Spiking Heidelberg Digits (SHD), and Spiking Google Speech Commands (SSC). Furthermore, we conduct a comprehensive study to demonstrate the superiority of the TC-LIF model in terms of remarkable temporal classification capability, effective long-term TCA, rapid training convergence, and high energy efficiency. Noted that the training of TC-LIF follows the BPTT with surrogate gradients (Nefcici, Mostafa, and Zenke 2019). More details about our experimental setups and training details are provided in Supplementary Materials.

### Parameter Space Exploration for Generalized Two-Compartment Neurons

Based on the P-R model, we have put forward a generalized two-compartment neuron model whose neuronal dynamics are governed by  $\{\alpha_1, \alpha_2, \beta_1, \beta_2\}$ . As discussed earlier, to alleviate the rapid decay of memory stored in membrane potentials, we set both  $\alpha_1$  and  $\alpha_2$  to one in the TC-LIF model. It is worth noting that the initialization of  $\beta_1$  and  $\beta_2$  will, however, significantly affect the training convergence of a two-compartment neuron model. To shed light on the effectiveness of the proposed parameter setting in the TC-LIF model, we conduct a grid search by initializing  $\beta_1$  and  $\beta_2$  across four different quadrants and evaluate their performance on the S-MNIST, PS-MNIST and GSC datasets.

In Figure 2, the dark blue line indicates the locations, where the partial derivative of the membrane potential between adjacent time steps  $\frac{\partial\mathcal{U}[j]}{\partial\mathcal{U}[j-1]}$  equals to one. As a result, the entire space of  $\beta$  is partitioned into two regions, wherein the third quadrant represents the region where the partial derivative is less than one. Conversely, the remaining three quadrants collectively represent the region where the partial derivative exceeds one. Within each quadrant, nine models are evaluated with equally spaced values for  $\beta_1$  and  $\beta_2$ , and the numerical annotations adjacent to these points indicate the model's test accuracy on the respective dataset.

The result reveals that apart from the models initialized in the second quadrant, models in other regions struggle to converge. Particularly, when we initialize  $\beta$  in the third quadrant, it refers to the scenario where the partial derivatives are less than 1 which leads to the gradient vanishing problem. In contrast, models with  $\beta$  initialized in the first quadrant

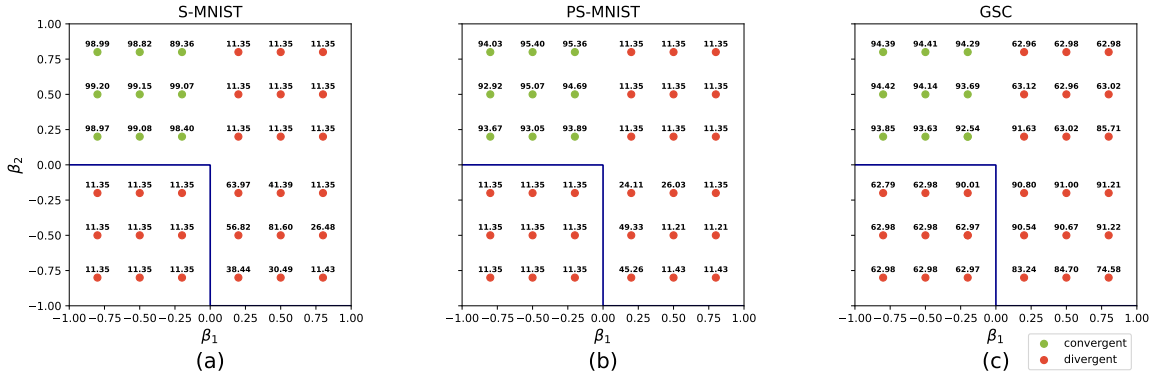


Figure 2: Study the impact of  $\beta_1$  and  $\beta_2$  initialization on the test accuracy of (a) S-MNIST, (b) PS-MNIST, and (c) GSC datasets. Note that on both S-MNIST and PS-MNIST datasets, the models initialized in the first and third quadrants face severe exploding and vanishing gradient problems, respectively. As a result, they are unable to learn any meaningful information and are thus stuck at an accuracy of 11.35%. The green dots refer to models that can converge to 100% training accuracy.

face the severe gradient exploding problem. Both the gradient vanishing and exploding problems impede network convergence. Note that these problems are less severe on the GSC dataset that is due to the significantly shorter sample duration, i.e.,  $T = 101$ . Although initializing  $\beta$  in the fourth quadrant can alleviate these problems, it results in a consistent negative input (see Eq. (11)) to the somatic compartment that will lead to poor temporal classification results as seen across all three tasks. Therefore, we initialize the values of  $\beta$  from the second quadrant, that is,  $\beta_1 \in (-1, 0)$  and  $\beta_2 \in (0, 1)$  for our TC-LIF model and we use it consistently for the rest of our experiments.

### Superior Temporal Classification Capability

Table 1 presents the results of the proposed TC-LIF model on five commonly used temporal classification datasets, along with other existing works. Overall, the TC-LIF model consistently outperforms SOTA single-compartment neuron models with a comparable amount of parameters.

For the S-MNIST dataset, each data sample has a sequence length of 784, which requires the model to learn long-term dependencies. As expected, the LIF model performs worst on this dataset, which can be explained by the vanishing gradient problem discussed earlier. Notably, the recently introduced adaptive spiking neuron model: LSNN (Bellec et al. 2018) and adaptive LIF (ALIF) (Yin, Corradi, and Bohté 2020, 2021) achieve comparable or even better accuracies to the LSTM model (Arjovsky, Shah, and Bengio 2016). Our proposed TC-LIF model consistently outperforms these single-compartment neuron models, indicating its effectiveness in retaining multiscale temporal information and handling long-term dependencies. Notably, we achieve 99.20% accuracy with a recurrent architecture, which is the best-reported SNN model for this dataset. The same conclusions can also be drawn for the more challenging PS-MNIST dataset.

In addition to image datasets, we further conduct experiments on speech datasets that exhibit richer temporal dy-

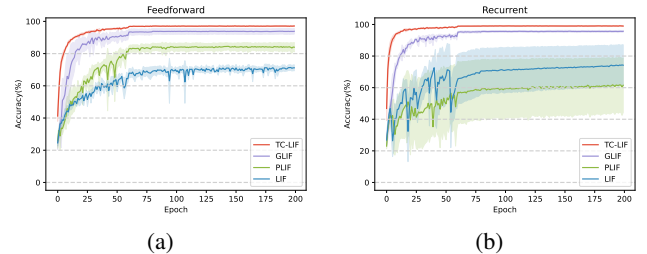


Figure 3: Comparison of the learning curves of TC-LIF and other single-compartment spiking neurons with (a) feedforward and (b) recurrent network architectures. Note that the mean and standard deviations across four runs are reported.

namics. For the non-spiking GSC dataset, our TC-LIF model achieves 90.57% and 94.42% accuracy for feedforward and recurrent networks respectively, surpassing SOTA models by a large margin. The SHD and SSC datasets are neuromorphic datasets that are specifically designed for benchmarking SNNs. On these datasets, our proposed TC-LIF exhibit a significant improvement over all other reported works.

### Effective Long-term Temporal Credit Assignment

To provide more insights into how long-term temporal relationship has been established in TC-LIF neurons, we visualize the error gradients calculated on the S-MNIST dataset. To enhance visual clarity, the gradient value  $\mathcal{G}_t^n$  of neuron  $n$  at time step  $t$  is normalized as  $\mathcal{G}_t^n / \sum_{i=0}^N \sum_{j=0}^T \mathcal{G}_j^i$ . As presented in Figure 4, TC-LIF neurons can effectively deliver more gradients to the earlier time steps as compared with LIF and ALIF models. This is more evident for the first and second layers (Neuron Index 1 – 320). These results suggest the exceptional ability of TC-LIF in performing long-term TCA.

Table 1: Comparison of model performance on S-MNIST, PS-MNIST, GSC, SHD, and SSC datasets.

| Datasets                               | Method   | SNN              | Network            | Parameters (K)     | Accuracy (%)       |
|--|--|------------------|--------------------|--------------------|--------------------|
| S-MNIST                                | GLIF* (Yao et al. 2022)                                | Y                | feedforward        | 47.1/87.5          | 94.80/95.27        |
|  | PLIF* (Fang et al. 2021b)                              | Y                | feedforward        | 44.8/85.1          | 83.71/87.92        |
|  | LIF*   | Y                | feedforward        | 44.8/85.1          | 62.42/72.06        |
|  | <b>TC-LIF (ours)</b>                                   | Y                | <b>feedforward</b> | <b>44.8/85.1</b>   | <b>96.46/97.35</b> |
|  | LSTM (non-spiking) (Arjovsky, Shah, and Bengio 2016)   | N                | recurrent          | 66.5/ -            | 98.20/ -           |
|  | SRNN+ReLU (non-spiking) (Yin, Corradi, and Bohté 2020) | Y                | recurrent          | 129.6/ -           | 98.99/ -           |
|  | LSNN (Bellec et al. 2018)                              | Y                | recurrent          | 68.2/ -            | 93.70/ -           |
|  | GLIF* (Yao et al. 2022)                                | Y                | recurrent          | 114.6/157.5        | 95.63/96.64        |
|  | SRNN+ALIF (Yin, Corradi, and Bohté 2020, 2021)         | Y                | recurrent          | 129.6/156.3        | 97.82/98.70        |
|  | PLIF* (Fang et al. 2021b)                              | Y                | recurrent          | 112.2/155.1        | 90.93/91.79        |
| LIF*                                   | Y  | recurrent        | 112.2/155.1        | 74.91/89.28        |                    |
| <b>TC-LIF (ours)</b>                   | Y  | <b>recurrent</b> | <b>63.6/155.1</b>  | <b>98.79/99.20</b> |                    |
| PS-MNIST                               | LIF*   | Y                | feedforward        | 44.8/85.1          | 11.30/10.00        |
|  | <b>TC-LIF (ours)</b>                                   | Y                | <b>feedforward</b> | <b>44.8/85.1</b>   | <b>80.89/83.98</b> |
|  | LSTM (non-spiking) (Arjovsky, Shah, and Bengio 2016)   | N                | recurrent          | 66.5/ -            | 88.00/ -           |
|  | SRNN+ReLU (non-spiking) (Yin, Corradi, and Bohté 2020) | N                | recurrent          | 129.6/ -           | 93.47/ -           |
|  | GLIF* (Yao et al. 2022)                                | Y                | recurrent          | 114.6/157.5        | 90.34/90.47        |
|  | SRNN+ALIF (Yin, Corradi, and Bohté 2020, 2021)         | Y                | recurrent          | 129.6/156.3        | 91.00/94.30        |
|  | LIF*   | Y                | recurrent          | 112.2/155.1        | 71.77/80.39        |
| <b>TC-LIF (ours)</b>                   | Y  | <b>recurrent</b> | <b>63.6/155.1</b>  | <b>92.69/95.36</b> |                    |
| GSC                                    | Rate-based SNN (Yilmaz et al. 2020)                    | Y                | feedforward        | 117                | 75.20              |
|  | <b>TC-LIF (ours)</b>                                   | Y                | <b>feedforward</b> | <b>106.2</b>       | <b>90.57</b>       |
|  | SRNN+ALIF (Yin, Corradi, and Bohté 2021)               | Y                | recurrent          | 221.7              | 92.10              |
|  | SNN (Salaj et al. 2021)                                | Y                | recurrent          | 4304.9             | 89.04              |
|  | SNN with SFA (Salaj et al. 2021)                       | Y                | recurrent          | 4307               | 91.21              |
| <b>TC-LIF (ours)</b>                   | Y  | <b>recurrent</b> | <b>196.5</b>       | <b>94.42</b>       |                    |
| SHD                                    | Feed-forward SNN (Cramer et al. 2020)                  | Y                | feedforward        | 108.8              | 48.60              |
|  | <b>TC-LIF (ours)</b>                                   | Y                | <b>feedforward</b> | <b>108.8</b>       | <b>83.08</b>       |
|  | SRNN (Cramer et al. 2020)                              | Y                | recurrent          | 108.8              | 71.4               |
|  | Heterogeneous SRNN (Perez-Nieves et al. 2021)          | Y                | recurrent          | 108.8              | 82.70              |
|  | Attention (Yao et al. 2021)                            | Y                | recurrent          | 133.8              | 81.45              |
|  | SRNN + ALIF (Yin, Corradi, and Bohté 2020)             | Y                | recurrent          | 142.4              | 84.40              |
|  | SRNN (Zenke and Vogels 2021)                           | Y                | recurrent          | 249                | 82.00              |
| SRNN + data augm. (Cramer et al. 2020) | Y  | recurrent        | 1787.9             | 83.20              |                    |
| <b>TC-LIF (ours)</b>                   | Y  | <b>recurrent</b> | <b>141.8</b>       | <b>88.91</b>       |                    |
| SSC                                    | Feed-forward SNN (Cramer et al. 2020)                  | Y                | feedforward        | 110.8              | 38.50              |
|  | <b>TC-LIF (ours)</b>                                   | Y                | <b>feedforward</b> | <b>110.8</b>       | <b>63.46</b>       |
|  | SRNN (Cramer et al. 2020)                              | Y                | recurrent          | 110.8              | 50.90              |
|  | Heterogeneous SRNN (Perez-Nieves et al. 2021)          | Y                | recurrent          | 110.8              | 57.3               |
|  | <b>TC-LIF (ours)</b>                                   | Y                | <b>recurrent</b>   | <b>110.8</b>       | <b>61.09</b>       |

\* Our reproduced results using publicly available codes.

## Rapid Training Convergence

Taking benefits of the exception ability in performing long-term TCA, the proposed TC-LIF model ensures more stable learning and faster network convergence. To shed light on this, we further compare the learning curves of the TC-LIF model alongside the LIF, GLIF, and PLIF models under the same training condition. As illustrated in Figure 3, the solid line denotes the mean accuracy, while the shaded area encapsulates the accuracy standard deviation across four runs with different random seeds. Notably, the TC-LIF model converges rapidly within about 25 epochs for both network structures, while the LIF model takes around 100 and 75 epochs to converge for feedforward and recurrent networks, respectively. Moreover, the TC-LIF model exhibits greater stability than other models, especially during the early training stage.

Furthermore, to investigate the reason why the TC-LIF model can achieve more stable learning and faster convergence, we further compare the loss landscape of LIF and TC-LIF near the founded local minima. As shown in Figure 5, it is obvious that the TC-LIF model exhibits a notably smoother loss landscape near the local minima. This suggests the TC-LIF model offers improved learning dynamics and convergence properties. In particular, the smoother loss landscape enables a reduced likelihood of being trapped into local minima, which can lead to more stable optimization and faster convergence. Additionally, the smoother loss landscape suggests stronger network generalization, as it is less prone to overfitting and underfitting problems.

## High Energy Efficiency

So far, it remains unclear whether the proposed TC-LIF model can make a good trade-off between model complexity



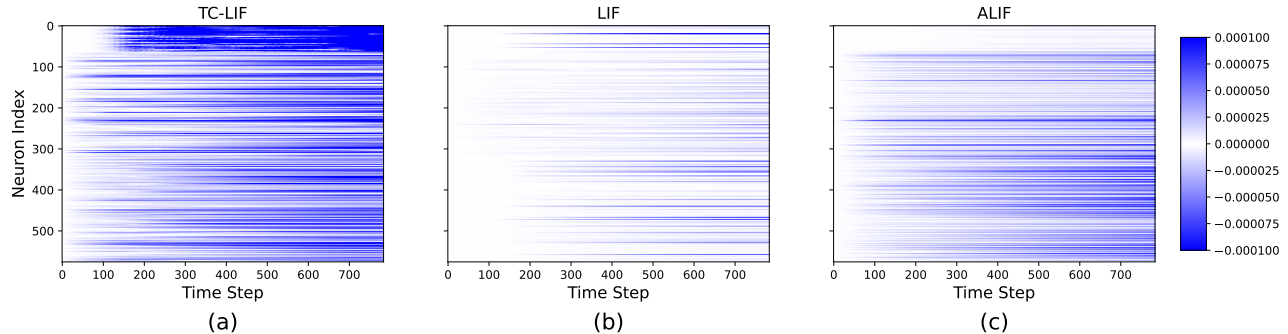


Figure 4: Illustration of the gradient evolution across time on the S-MNIST dataset. Note that the gradient has been calculated on a random batch of 256 samples with a three-layer feedforward SNN (64-256-256).

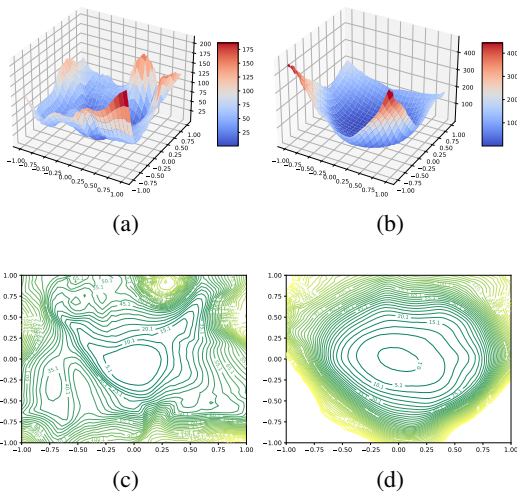


Figure 5: Comparison of the loss landscape of (a, c) LIF and (b, d) TC-LIF neuron models in terms of 3D surface and 2D contour plots.

and computational efficiency. To answer this question, we analyze and compare the energy efficiency of LIF, TC-LIF, and LSTM models. In particular, we count the accumulated (AC) and multiply-and-accumulate (MAC) operations consumed during input data processing and network update. In ANNs, the computations are all performed with MAC operations, whereas the AC operations are used predominantly in SNNs for synaptic updates. It is worth noting that the membrane potential update of spiking neurons requires several MAC operations. More detailed calculations can be found in Supplementary Materials.

As the theoretical results presented in Table 2, the energy costs of both spiking neurons (i.e., LIF and TC-LIF) are significantly lower than that of the LSTM model, attributed to their reduced computational complexity. Compared to the LIF model, the proposed TC-LIF model incurs additional

$nFr_{out}E_{AC} + nE_{MAC}$  operations due to the extra computations at the dendritic compartment. To calculate the empirical energy cost, we perform inference on one randomly selected batch of test samples and compute the average layer-wise firing rates of these SNNs on the S-MNIST dataset. The layer-wise firing rates for LIF and TC-LIF models are comparable that take the values of [0.219, 0.145, 0.004] and [0.294, 0.146, 0.030], respectively. To obtain the total energy cost, we base our calculation on the 45nm CMOS process that has an estimated cost of  $E_{AC} = 0.9 pJ$  and  $E_{MAC} = 4.6 pJ$  for AC and MAC operations, respectively (Horowitz 2014). Despite the more complex internal structure of the proposed TC-LIF model, it has a comparable energy cost to the LIF model. Remarkably, our TC-LIF model achieves more than 100 times energy savings compared with the LSTM model, while demonstrating superior temporal classification performance.

Table 2: Comparison of the theoretical and empirical energy cost of LIF, LSTM, and TC-LIF models. The  $m$  and  $n$  are the numbers of input and output neurons.  $Fr_{in}$  and  $Fr_{out}$  are the firing rate of input and output neurons.  $E_{AC}$  and  $E_{MAC}$  are the energy cost of MAC and AC operations.

| Neuron Model | Theoretical Energy Cost                                 | Empirical Energy Cost (nJ) |
|--------------|---|----------------------------|
| LSTM         | $4(mn + nn)E_{MAC} + 17nE_{MAC}$                        | 2,834.7                    |
| LIF          | $mnFr_{in}E_{AC} + (nm + n)Fr_{out}E_{AC} + nE_{MAC}$   | 23.8                       |
| TC-LIF       | $mnFr_{in}E_{AC} + (nn + 2n)Fr_{out}E_{AC} + 2nE_{MAC}$ | 28.2                       |

## Conclusion

In this paper, drawing inspiration from the multi-compartment structure of biological neurons, we proposed a novel TC-LIF neuron to enhance the long-term sequential modeling capability of spiking neurons. The dendritic and somatic compartments of the proposed TC-LIF model synergistically interact, enriching neuronal dynamics and effectively addressing the TCA problem when properly configured. Theoretical analysis and experimental results on

various temporal classification tasks demonstrate the superiority of the proposed TC-LIF model, including superior temporal classification capability, effective long-term TCA, rapid training convergence, and high energy efficiency. This work, therefore, contributes to the development of more effective and efficient spiking neurons for solving sequential modeling tasks. In this work, we focus our study on two-compartment neuron models, while how to generalize the design to more compartments remains an interesting question that we will explore in future works.

## References

- Abbott, L. F.; and Kepler, T. B. 2005. Model neurons: from Hodgkin-Huxley to Hopfield. In *Statistical Mechanics of Neural Networks: Proceedings of the XIth Sitges Conference Sitges, Barcelona, Spain, 3–7 June 1990*, 5–18. Springer.
- Arjovsky, M.; Shah, A.; and Bengio, Y. 2016. Unitary evolution recurrent neural networks. In *International conference on machine learning*, 1120–1128. PMLR.
- Beaulieu-Laroche, L.; Toloza, E. H.; Brown, N. J.; and Harnett, M. T. 2019. Widespread and highly correlated somatodendritic activity in cortical layer 5 neurons. *Neuron*, 103(2): 235–241.
- Bellec, G.; Salaj, D.; Subramoney, A.; Legenstein, R.; and Maass, W. 2018. Long short-term memory and learning-to-learn in networks of spiking neurons. *Advances in neural information processing systems*, 31.
- Bellec, G.; Scherr, F.; Subramoney, A.; Hajek, E.; Salaj, D.; Legenstein, R.; and Maass, W. 2020. A solution to the learning dilemma for recurrent networks of spiking neurons. *Nature communications*, 11(1): 3625.
- Brette, R.; and Gerstner, W. 2005. Adaptive exponential integrate-and-fire model as an effective description of neuronal activity. *Journal of neurophysiology*, 94(5): 3637–3642.
- Brown, T.; Mann, B.; Ryder, N.; Subbiah, M.; Kaplan, J. D.; Dhariwal, P.; Neelakantan, A.; Shyam, P.; Sastry, G.; Askell, A.; et al. 2020. Language models are few-shot learners. *Advances in neural information processing systems*, 33: 1877–1901.
- Bu, T.; Fang, W.; Ding, J.; Dai, P.; Yu, Z.; and Huang, T. 2023. Optimal ANN-SNN conversion for high-accuracy and ultra-low-latency spiking neural networks. *arXiv preprint arXiv:2303.04347*.
- Chakraborty, B.; and Mukhopadhyay, S. 2023. Heterogeneous Neuronal and Synaptic Dynamics for Spike-Efficient Unsupervised Learning: Theory and Design Principles. *arXiv preprint arXiv:2302.11618*.
- Che, K.; Leng, L.; Zhang, K.; Zhang, J.; Meng, Q.; Cheng, J.; Guo, Q.; and Liao, J. 2022. Differentiable hierarchical and surrogate gradient search for spiking neural networks. *Advances in Neural Information Processing Systems*, 35: 24975–24990.
- Chen, Y.; Zhang, S.; Ren, S.; and Qu, H. 2022. Gradual Surrogate Gradient Learning in Deep Spiking Neural Networks. In *ICASSP 2022–2022 IEEE International Conference on Acoustics, Speech and Signal Processing (ICASSP)*, 8927–8931. IEEE.
- Cichon, J.; and Gan, W.-B. 2015. Branch-specific dendritic Ca<sup>2+</sup> spikes cause persistent synaptic plasticity. *Nature*, 520(7546): 180–185.
- Cramer, B.; Stradmann, Y.; Schemmel, J.; and Zenke, F. 2020. The Heidelberg spiking data sets for the systematic evaluation of spiking neural networks. *IEEE Transactions on Neural Networks and Learning Systems*, 33(7): 2744–2757.
- Davies, M.; Srinivasa, N.; Lin, T.-H.; Chinya, G.; Cao, Y.; Choday, S. H.; Dimou, G.; Joshi, P.; Imam, N.; Jain, S.; et al. 2018. Loihi: A neuromorphic manycore processor with on-chip learning. *Ieee Micro*, 38(1): 82–99.
- Devlin, J.; Chang, M.-W.; Lee, K.; and Toutanova, K. 2018. Bert: Pre-training of deep bidirectional transformers for language understanding. *arXiv preprint arXiv:1810.04805*.
- Duan, C.; Ding, J.; Chen, S.; Yu, Z.; and Huang, T. 2022. Temporal effective batch normalization in spiking neural networks. *Advances in Neural Information Processing Systems*, 35: 34377–34390.
- Fang, W.; Yu, Z.; Chen, Y.; Huang, T.; Masquelier, T.; and Tian, Y. 2021a. Deep residual learning in spiking neural networks. *Advances in Neural Information Processing Systems*, 34: 21056–21069.
- Fang, W.; Yu, Z.; Chen, Y.; Masquelier, T.; Huang, T.; and Tian, Y. 2021b. Incorporating learnable membrane time constant to enhance learning of spiking neural networks. In *Proceedings of the IEEE/CVF International Conference on Computer Vision*, 2661–2671.
- Feng, L.; Liu, Q.; Tang, H.; Ma, D.; and Pan, G. 2022. Multi-Level Firing with Spiking DS-ResNet: Enabling Better and Deeper Directly-Trained Spiking Neural Networks. *arXiv preprint arXiv:2210.06386*.
- Furber, S. B.; Galluppi, F.; Temple, S.; and Plana, L. A. 2014. The spinnaker project. *Proceedings of the IEEE*, 102(5): 652–665.
- Gast, R.; Solla, S. A.; and Kennedy, A. 2022. Effects of Neural Heterogeneity on Spiking Neural Network Dynamics. *arXiv preprint arXiv:2206.08813*.
- Gerstner, W.; Kistler, W. M.; Naud, R.; and Paninski, L. 2014. *Neuronal dynamics: From single neurons to networks and models of cognition*. Cambridge University Press.
- Gidon, A.; and Segev, I. 2012. Principles governing the operation of synaptic inhibition in dendrites. *Neuron*, 75(2): 330–341.
- Graves, A.; and Graves, A. 2012. Long short-term memory. *Supervised sequence labelling with recurrent neural networks*, 37–45.
- Graves, A.; Mohamed, A.-r.; and Hinton, G. 2013. Speech recognition with deep recurrent neural networks. In *2013 IEEE international conference on acoustics, speech and signal processing*, 6645–6649. Ieee.
- Gulati, A.; Qin, J.; Chiu, C.-C.; Parmar, N.; Zhang, Y.; Yu, J.; Han, W.; Wang, S.; Zhang, Z.; Wu, Y.; et al. 2020.



- Conformer: Convolution-augmented transformer for speech recognition. *arXiv preprint arXiv:2005.08100*.
- Guo, Y.; Chen, Y.; Zhang, L.; Liu, X.; Wang, Y.; Huang, X.; and Ma, Z. 2022. IM-loss: information maximization loss for spiking neural networks. *Advances in Neural Information Processing Systems*, 35: 156–166.
- Hausser, M.; Spruston, N.; and Stuart, G. J. 2000. Diversity and dynamics of dendritic signaling. *Science*, 290(5492): 739–744.
- He, K.; Chen, X.; Xie, S.; Li, Y.; Dollár, P.; and Girshick, R. 2022. Masked autoencoders are scalable vision learners. In *Proceedings of the IEEE/CVF Conference on Computer Vision and Pattern Recognition*, 16000–16009.
- He, Y.; Sainath, T. N.; Prabhavalkar, R.; McGraw, I.; Alvarez, R.; Zhao, D.; Rybach, D.; Kannan, A.; Wu, Y.; Pang, R.; et al. 2019. Streaming end-to-end speech recognition for mobile devices. In *ICASSP 2019-2019 IEEE International Conference on Acoustics, Speech and Signal Processing (ICASSP)*, 6381–6385. IEEE.
- Hodgkin, A. L.; and Huxley, A. F. 1952. A quantitative description of membrane current and its application to conduction and excitation in nerve. *The Journal of physiology*, 117(4): 500.
- Horowitz, M. 2014. 1.1 computing’s energy problem (and what we can do about it). In *2014 IEEE International Solid-State Circuits Conference Digest of Technical Papers (ISSCC)*, 10–14. IEEE.
- Hu, Y.; Wu, Y.; Deng, L.; and Li, G. 2021. Advancing residual learning towards powerful deep spiking neural networks. *arXiv preprint arXiv:2112.08954*.
- Ikegawa, S.-i.; Saiin, R.; Sawada, Y.; and Natori, N. 2022. Rethinking the role of normalization and residual blocks for spiking neural networks. *Sensors*, 22(8): 2876.
- Izhikevich, E. M. 2003. Simple model of spiking neurons. *IEEE Transactions on neural networks*, 14(6): 1569–1572.
- Kim, Y.; and Panda, P. 2021. Revisiting batch normalization for training low-latency deep spiking neural networks from scratch. *Frontiers in neuroscience*, 1638.
- Krizhevsky, A.; Sutskever, I.; and Hinton, G. E. 2017. ImageNet classification with deep convolutional neural networks. *Communications of the ACM*, 60(6): 84–90.
- Le, Q. V.; Jaitly, N.; and Hinton, G. E. 2015. A simple way to initialize recurrent networks of rectified linear units. *arXiv preprint arXiv:1504.00941*.
- LeCun, Y.; Bengio, Y.; and Hinton, G. 2015. Deep learning. *nature*, 521(7553): 436–444.
- LeCun, Y.; Bottou, L.; Bengio, Y.; and Haffner, P. 1998. Gradient-based learning applied to document recognition. *Proceedings of the IEEE*, 86(11): 2278–2324.
- Lin, Q.; Wang, J.; Yang, S.; Yi, G.; Deng, B.; Wei, X.; and Yu, H. 2017. The dynamical analysis of modified two-compartment neuron model and FPGA implementation. *Physica A: Statistical Mechanics and its Applications*, 484: 199–214.
- London, M.; and Häusser, M. 2005. Dendritic computation. *Annu. Rev. Neurosci.*, 28: 503–532.
- Luo, L. 2021. Architectures of neuronal circuits. *Science*, 373(6559): eabg7285.
- Maass, W. 1997. Networks of spiking neurons: the third generation of neural network models. *Neural networks*, 10(9): 1659–1671.
- Maass, W.; Natschläger, T.; and Markram, H. 2002. A model for real-time computation in generic neural microcircuits. *Advances in neural information processing systems*, 15.
- Markram, H.; Müller, E.; Ramaswamy, S.; Reimann, M. W.; Abdellah, M.; Sanchez, C. A.; Ailamaki, A.; Alonso-Nanclares, L.; Antille, N.; Arsever, S.; et al. 2015. Reconstruction and simulation of neocortical microcircuitry. *Cell*, 163(2): 456–492.
- Neftci, E. O.; Mostafa, H.; and Zenke, F. 2019. Surrogate gradient learning in spiking neural networks: Bringing the power of gradient-based optimization to spiking neural networks. *IEEE Signal Processing Magazine*, 36(6): 51–63.
- Panda, P.; and Roy, K. 2017. Learning to generate sequences with combination of hebbian and non-hebbian plasticity in recurrent spiking neural networks. *Frontiers in neuroscience*, 11: 693.
- Pei, J.; Deng, L.; Song, S.; Zhao, M.; Zhang, Y.; Wu, S.; Wang, G.; Zou, Z.; Wu, Z.; He, W.; et al. 2019. Towards artificial general intelligence with hybrid Tianjic chip architecture. *Nature*, 572(7767): 106–111.
- Perez-Nieves, N.; Leung, V. C.; Dragotti, P. L.; and Goodman, D. F. 2021. Neural heterogeneity promotes robust learning. *Nature communications*, 12(1): 5791.
- Pfeiffer, M.; and Pfeil, T. 2018. Deep learning with spiking neurons: Opportunities and challenges. *Frontiers in neuroscience*, 12: 774.
- Pinsky, P. F.; and Rinzel, J. 1994. Intrinsic and network rhythmogenesis in a reduced Traub model for CA3 neurons. *Journal of computational neuroscience*, 1: 39–60.
- Qin, L.; Wang, Z.; Yan, R.; and Tang, H. 2023. Attention-Based Deep Spiking Neural Networks for Temporal Credit Assignment Problems. *IEEE Transactions on Neural Networks and Learning Systems*.
- Radford, A.; Wu, J.; Child, R.; Luan, D.; Amodei, D.; Sutskever, I.; et al. 2019. Language models are unsupervised multitask learners. *OpenAI blog*, 1(8): 9.
- Rall, W. 1964. Theoretical significance of dendritic trees for neuronal input-output relations. *Neural theory and modeling*, 73–97.
- Salaj, D.; Subramoney, A.; Krausnikovic, C.; Bellec, G.; Legenstein, R.; and Maass, W. 2021. Spike frequency adaptation supports network computations on temporally dispersed information. *Elife*, 10: e65459.
- Shaban, A.; Bezugam, S. S.; and Suri, M. 2021. An adaptive threshold neuron for recurrent spiking neural networks with nanodevice hardware implementation. *Nature Communications*, 12(1): 4234.
- Stuart, G. J.; and Spruston, N. 2015. Dendritic integration: 60 years of progress. *Nature neuroscience*, 18(12): 1713–1721.

- Tan, M.; Pang, R.; and Le, Q. V. 2020. Efficientdet: Scalable and efficient object detection. In *Proceedings of the IEEE/CVF conference on computer vision and pattern recognition*, 10781–10790.
- Tavanaei, A.; Ghodrati, M.; Kheradpisheh, S. R.; Masquelier, T.; and Maida, A. 2019. Deep learning in spiking neural networks. *Neural networks*, 111: 47–63.
- Ujfalussy, B. B.; Makara, J. K.; Branco, T.; and Lengyel, M. 2015. Dendritic nonlinearities are tuned for efficient spike-based computations in cortical circuits. *Elife*, 4: e10056.
- Warden, P. 2018. Speech commands: A dataset for limited-vocabulary speech recognition. *arXiv preprint arXiv:1804.03209*.
- Wu, J.; Xu, C.; Han, X.; Zhou, D.; Zhang, M.; Li, H.; and Tan, K. C. 2021. Progressive tandem learning for pattern recognition with deep spiking neural networks. *IEEE Transactions on Pattern Analysis and Machine Intelligence*, 44(11): 7824–7840.
- Wu, Y.; Deng, L.; Li, G.; Zhu, J.; and Shi, L. 2018. Spatio-temporal backpropagation for training high-performance spiking neural networks. *Frontiers in neuroscience*, 12: 331.
- Yang, Q.; Wu, J.; Zhang, M.; Chua, Y.; Wang, X.; and Li, H. 2022. Training Spiking Neural Networks with Local Tandem Learning. *arXiv preprint arXiv:2210.04532*.
- Yao, M.; Gao, H.; Zhao, G.; Wang, D.; Lin, Y.; Yang, Z.; and Li, G. 2021. Temporal-wise attention spiking neural networks for event streams classification. In *Proceedings of the IEEE/CVF International Conference on Computer Vision*, 10221–10230.
- Yao, X.; Li, F.; Mo, Z.; and Cheng, J. 2022. GLIF: A Unified Gated Leaky Integrate-and-Fire Neuron for Spiking Neural Networks. *arXiv preprint arXiv:2210.13768*.
- Yi, G.; Wang, J.; Tsang, K.-M.; Wei, X.; Deng, B.; and Han, C. 2015. Spike-frequency adaptation of a two-compartment neuron modulated by extracellular electric fields. *Biological Cybernetics*, 109(3): 287–306.
- Yilmaz, E.; Gevrek, O. B.; Wu, J.; Chen, Y.; Meng, X.; and Li, H. 2020. Deep convolutional spiking neural networks for keyword spotting. In *Proceedings of INTERSPEECH*, 2557–2561.
- Yin, B.; Corradi, F.; and Bohté, S. M. 2020. Effective and efficient computation with multiple-timescale spiking recurrent neural networks. In *International Conference on Neuromorphic Systems 2020*, 1–8.
- Yin, B.; Corradi, F.; and Bohté, S. M. 2021. Accurate and efficient time-domain classification with adaptive spiking recurrent neural networks. *Nature Machine Intelligence*, 3(10): 905–913.
- Zenke, F.; and Vogels, T. P. 2021. The remarkable robustness of surrogate gradient learning for instilling complex function in spiking neural networks. *Neural computation*, 33(4): 899–925.
- Zhang, M.; Wang, J.; Wu, J.; Belatreche, A.; Amornpaisannon, B.; Zhang, Z.; Miriyala, V. P. K.; Qu, H.; Chua, Y.; Carlson, T. E.; et al. 2021. Rectified linear postsynaptic potential function for backpropagation in deep spiking neural networks. *IEEE transactions on neural networks and learning systems*, 33(5): 1947–1958.
- Zheng, H.; Wu, Y.; Deng, L.; Hu, Y.; and Li, G. 2021. Going deeper with directly-trained larger spiking neural networks. In *Proceedings of the AAAI Conference on Artificial Intelligence*, volume 35, 11062–11070.

## Supplementary Materials

### Two-Compartment Biological Prinsky-Rinzel Neuron Model

In this paper, we utilized the simplified Prinsky-Rinzel (P-R) neuron model proposed by Kepecs and Wang. This model represents a pyramidal cell in the CA3 region with two compartments - the somatic and dendritic compartments. The dendritic compartment is responsible for producing bursting responses, while the soma generates spikes. The somatic compartment is governed by the  $I_{Na}$  and  $I_K$  currents, whereas the dendritic compartment is characterized by the slow potassium  $I_{KS}$  and a persistent sodium  $I_{NaP}$  currents. The P-R neuron model consists of several parameters and two-compartment coupled equations, mathematically described by:

$$C_m \frac{dV_s}{dt} = -I_{Na} - I_K - I_{Leak} + \frac{I_{link}}{P} + I_s \quad (17)$$

$$C_m \frac{dV_d}{dt} = -I_{NaP} - I_{KS} - I_{Leak} - \frac{I_{link}}{1-P} + I_d \quad (18)$$

where  $V_s$  and  $V_d$  are the somatic and dendritic membrane potentials,  $I_d$  and  $I_s$  denote the currents applied to the soma and dendrite, respectively. Specifically,  $I_s$  is assumed to be 0 in this paper and dendrite is the only part in neuron model to accept the outer currents. The membrane capacitance and the proportion of the cell area taken by soma are respectively denoted by  $C_m$  and  $P$ . In the Table 4, the ionic currents participate in Equations 17, 18 and their corresponding calculations are presented. In the computations of ionic currents,  $E_{Na}$ ,  $E_K$  and  $E_L$  represent equilibrium potentials, and  $g_{Na}$ ,  $g_K$ ,  $g_L$ ,  $g_c$ ,  $g_{NaP}$  and  $g_{KS}$  are conductances.

Following the Equations 17 and 18 in the continuous time, the iterative and discrete-time forms are obtained through Euler method:

$$V_s[t+1] = V_s[t] + \frac{dt}{C_m} (-I_{Na}[t] - I_K[t] - I_{Leak}[t] + \frac{I_{link}[t]}{P} + I_s) \quad (19)$$

$$V_d[t+1] = V_d[t] + \frac{dt}{C_m} (-I_{NaP}[t] - I_{KS}[t] - I_{Leak}[t] - \frac{I_{link}[t]}{1-P} + I_d) \quad (20)$$

The term  $I_{link}$  encompasses the interaction between the somatic and dendritic compartments in the membrane potential. Furthermore, by incorporating the reset operation in the somatic output to transform the neuron into a spiking form, we deduce the overall dynamics of the two-compartment P-R spiking neuron model, as shown in Equations 7, 8 and 9.

### Study on Energy Efficiency

We analyze the theoretical energy cost for LSTM, LIF, and TC-LIF recurrent networks based on their neuronal dynamics update functions. Table 3 presents the detailed calculation of theoretical energy cost for each model.

## Experimental Details

### Datasets

In this subsection, we introduce the dataset used for this work. These datasets cover a wide range of tasks, allowing us to assess the model’s capabilities in handling different types of input data.

**S-MNIST:** The Sequential-MNIST (S-MNIST) dataset is derived from the original MNIST dataset, which consists of 60,000 and 10,000 grayscale images of handwritten digits for training and testing sets with a resolution of  $28 \times 28$  pixels. In the S-MNIST dataset, each image is converted into a vector of 784 time steps, with each pixel representing one input value at a certain time step. This dataset enables us to evaluate the performance of our model in solving sequential image classification tasks.

**PS-MNIST:** The Permuted Sequential MNIST dataset (PS-MNIST) is a variation of the Sequential MNIST dataset, in which the pixels in each image are shuffled according to a fixed random permutation. This dataset provides a more challenging task than S-MNIST, as the input sequences no longer follow the original spatial order of the images. Therefore, when learning this dataset, the model needs to capture complex, non-local, and long-term dependencies between pixels.

**GSC:** The Google Speech Commands (GSC) has two versions, and we employ the 2nd version in this work. The GSC version 2 is a collection of 105,829 on-second-long audio clips of 35 different spoken commands, such as “yes”, “no”, “up”, “down”, “left”, “right”, etc. These audio clips are recorded by different speakers in various environments, offering a diversity of datasets to evaluate the performance of our model.

**SHD:** The Spiking Heidelberg Digits dataset is a spike-based sequence classification benchmark, consisting of spoken digits from 0 to 9 in both English and German (20 classes). The dataset contains recordings from twelve different speakers, with two of them only appearing in the test set. Each original waveform has been converted into spike trains over 700 input channels. The train set contains 8,332 examples, and the test set consists of 2,088 examples (no validation set). The SHD dataset enables us to evaluate the performance of our proposed model in processing and classifying speech data represented in spiking format.

**SSC:** The Spiking Speech Command dataset, another spike-based sequence classification benchmark, is derived from the Google Speech Commands version 2 dataset and contains 35 classes from a large number of speakers. The original waveforms have been converted to spike trains over 700 input channels. The dataset is divided into train, validation, and test splits, with 75,466, 9,981, and 20,382 examples, respectively. The SSC dataset allows us to assess the performance of our proposed spiking neuron model in processing and recognizing speech commands represented in spiking data.

### Training with surrogate gradient

Training SNN poses challenges stemming from the non-differentiability of spike functions, denoted as  $\Theta(x)$  in

Table 3: Computations on the energy cost of LIF, TC-LIF, and LSTM.

| Neuron Model | Dynamics   | Step Cost  | Total Cost   |
|--------------|--|--|--|
| LIF          | $\mathcal{I}_t = \mathcal{W}^{m,n} X^m + \mathcal{W}^{n,n} \mathcal{S}_{t-1}^n$<br>$\mathcal{U}_t = \beta \mathcal{U}_{t-1} + \mathcal{I}_t - \mathcal{V}_{th} \mathcal{S}_{t-1}^n$  | $(mnFr_{in} + nnFr_{out})E_{AC}$<br>$nFr_{out}E_{AC} + nE_{MAC}$   | $mnFr_{in}E_{AC} + (nn + n)Fr_{out}E_{AC}$<br>$+ nE_{MAC}$       |
| TC-LIF       | $\mathcal{I}_t = \mathcal{W}^{m,n} X^m + \mathcal{W}^{n,n} \mathcal{S}_{t-1}^n$<br>$\mathcal{U}_t^D = \mathcal{U}_{t-1}^D + \mathcal{I}_t + \beta_1 \mathcal{U}_{t-1}^S - \gamma \mathcal{S}_{t-1}^n$<br>$\mathcal{U}_t^S = \mathcal{U}_{t-1}^S + \beta_2 \mathcal{U}_t^D - \mathcal{V}_{th} \mathcal{S}_{t-1}^n$                    | $(mnFr_{in} + nnFr_{out})E_{AC}$<br>$nFr_{out}E_{AC} + nE_{MAC}$<br>$nFr_{out}E_{AC} + nE_{MAC}$                               | $mnFr_{in}E_{AC}$<br>$+(nn + 2n)Fr_{out}E_{AC}$<br>$+ 2nE_{MAC}$ |
| LSTM         | $f_t = \sigma_g(\mathcal{W}_f x_t + U_f h_{t-1} + b_f)$<br>$i_t = \sigma_g(\mathcal{W}_i x_t + U_i h_{t-1} + b_i)$<br>$o_t = \sigma_g(\mathcal{W}_o x_t + U_o h_{t-1} + b_o)$<br>$\hat{c}_t = \sigma_c(\mathcal{W}_c x_t + U_c h_{t-1} + b_c)$<br>$c_t = f_t \odot c_{t-1} + i_t \odot \hat{c}_t$<br>$h_t = o_t \odot \sigma_h(c_t)$ | $n(m + n + 2)E_{MAC}$<br>$n(m + n + 2)E_{MAC}$<br>$n(m + n + 2)E_{MAC}$<br>$n(m + n + 4)E_{MAC}$<br>$2nE_{MAC}$<br>$5nE_{MAC}$ | $4(mn + nn)E_{MAC}$<br>$17nE_{MAC}$                              |

Eq.(3, 9 and 12). This trait hinders the application of prevalent gradient-based optimization methods, notably backpropagation. The surrogate gradient approach offers a solution to this impediment by introducing a proxy gradient as an approximation for the gradient of the spike function, expressed as  $\Theta'(x) \approx \theta'(x)$ . While the actual gradient mostly holds a zero value, the surrogate gradient approximates non-zero values in regions of interest. This allows backpropagation to be applied, as the surrogate gradient provides the necessary feedback to update the network’s weight.

In this work, we adopt the triangle function as  $\theta'(x)$  to enable gradient-based training for SNN:

$$\frac{\partial \mathcal{S}[t]}{\partial \mathcal{U}[t]} = \theta'(\mathcal{U}[t] - \mathcal{V}_{th}) = \max(1 - |\mathcal{U}[t] - \mathcal{V}_{th}|, 0) \quad (21)$$

where  $\mathcal{U}[t]$  denotes the membrane potential in Eq. (3) for single-compartment spiking neuron and the somatic membrane potential in Eq. (9) and (12) for two-compartment spiking neurons.

## Network Architecture

We perform experiments employing both feedforward and recurrent connection configurations. To maintain a fair comparison with existing works, we utilize network architectures exhibiting comparable parameters. These architectures and their corresponding parameters are summarized in Table 6.

Table 4: Calculations of ionic currents in P-R neuron model.

| Ionic Current | Calculation                         | Ionic Current | Calculation                          |
|---------------|-------------------------------------|---------------|--------------------------------------|
| $I_{Na}$      | $g_{Na} m^3 h \cdot (V_s - E_{Na})$ | $I_{inK}$     | $g_c \cdot (V_d - V_s)$              |
| $I_K$         | $g_K n^4 \cdot (V_s - E_K)$         | $I_{NaP}$     | $g_{NaP} l^3 h \cdot (V_d - E_{Na})$ |
| $I_{Leak}$    | $g_L \cdot (V - E_L)$               | $I_{KS}$      | $g_{KS} s q \cdot (V_d - E_K)$       |

## TC-LIF Model Hyper-parameters

In this section, we provide our detailed settings on the hyper-parameters of TC-LIF neuron model in Table 5, including the  $\gamma$ , initial values of  $\beta$  and neuronal threshold  $\mathcal{V}_{th}$ .

## Training Configuration

We train the S-MNIST and PS-MNIST datasets for 200 epochs utilizing the Adam optimizer. Their initial learning rates are set to 0.0005 for both feedforward and recurrent

Table 5: Training hyper-parameters for TC-LIF.

| Dataset  | Network     | $\gamma$ | $\beta$     | $\mathcal{V}_{th}$ |
|----------|-------------|----------|-------------|--------------------|
| S-MNIST  | feedforward | 0.5      | (-0.5, 0.5) | 1.0                |
|          | recurrent   | 0.5      | (-0.5, 0.5) | 1.0                |
| PS-MNIST | feedforward | 0.7      | (-0.5, 0.5) | 1.5                |
|          | recurrent   | 1.0      | (-0.2, 0.8) | 1.8                |
| GSC      | feedforward | 0.6      | (-0.5, 0.5) | 1.2                |
|          | recurrent   | 0.6      | (-0.7, 0.7) | 1.3                |
| SHD      | feedforward | 0.5      | (-0.5, 0.5) | 1.5                |
|          | recurrent   | 0.5      | (-0.5, 0.5) | 1.5                |
| SSC      | feedforward | 0.5      | (-0.5, 0.5) | 1.5                |
|          | recurrent   | 0.5      | (-0.5, 0.5) | 1.5                |

Table 6: Summary of network architectures and parameters.

| Dataset  | Network     | Architecture                 | Parameters(K) |
|----------|-------------|------------------------------|---------------|
| S-MNIST  | feedforward | 40-256-128-10/ 64-256-256-10 | 44.8/ 85.1    |
|          | recurrent   | 40-200-64-10/ 64-256-256-10  | 63.6/ 155.1   |
| PS-MNIST | feedforward | 40-256-128-10/ 64-256-256-10 | 44.8/ 85.1    |
|          | recurrent   | 40-200-64-10/ 64-256-256-10  | 63.6/ 155.1   |
| GSC      | feedforward | 40-300-30-12                 | 106.2         |
|          | recurrent   | 40-300-30-12                 | 106.2         |
| SHD      | feedforward | 700-128-128-20               | 108.8         |
|          | recurrent   | 700-128-128-20               | 108.8         |
| SSC      | feedforward | 700-128-128-135              | 110.8         |
|          | recurrent   | 700-128-128-135              | 110.8         |

networks with the learning rates decaying by a factor of 10 at epochs 60 and 80. For the GSC, SHD, and SSC datasets, we train the models for 100 epochs using the Adam optimizer. The initial learning rate of GSC datasets is 0.001 for both feedforward and recurrent networks with the decaying by 10 at epochs 60, 90, and 120. The initial learning rate is set to 0.0005, and 0.005 for feedforward and recurrent networks on the SHD dataset, with the learning rate decaying to 0.8 times its previous value every 10 epochs. For the SSC dataset, the initial learning rates are 0.0001 for both feedforward and recurrent networks, and decay to 0.8 times their previous values every 10 epochs. We train S-MNIST, PS-MNIST, and GSC tasks on Nvidia Geforce GTX 3090Ti GPUs with 24GB memory, and train SHD and SSC tasks on

Nvidia Geforce GTX 1080Ti GPUs with 12GB memory.

### Source Code

All codes to reproduce our results will be released after the reviewing process.

### Gradient Exploding Problem Analysis

Here, we analyze the severity of the gradient exploding problem for a number of  $\beta$  values selected from the second quadrant. In particular, we train recurrent TC-LIF models on the S-MNIST dataset with the selected  $\beta$  parameters, and we record the learnable  $\beta$  parameters before and after the training process as well as the corresponding infinite norm of partial derivative in the last hidden layer.

We notice that, except for the case where the initialization is at  $(-0.2, 0.8)$  with a corresponding infinite norm of 2.36, the remaining models have yielded relatively satisfactory results. While the observation that the infinite norm of the partial derivative surpasses 1 implies the potential for the exploding gradient problem during long-term BPTT, our experimental results indicate that a value slightly above 1 for the infinite norm does not significantly impede convergence. Fortunately, for the majority of the  $\beta$  values in the second quadrant, the values of the infinite norm met this condition. Therefore, when initializing the TC-LIF model within this quadrant, it ensures stable convergence for the proposed TC-LIF model.

Table 7: Calculations related to  $\beta$  when TC-LIF converges on S-MNIST.

| Initial $\beta$ | Convergent $\beta$ | Infinite Norm | Accuracy |
|-----------------|--------------------|---------------|----------|
| $(-0.2, 0.2)$   | $(-0.184, 0.146)$  | 1.262         | 98.40    |
| $(-0.2, 0.4)$   | $(-0.188, 0.307)$  | 1.539         | 99.07    |
| $(-0.2, 0.6)$   | $(-0.203, 0.563)$  | 1.948         | 99.15    |
| $(-0.2, 0.8)$   | $(-0.202, 0.835)$  | 2.360         | 89.36    |
| $(-0.4, 0.2)$   | $(-0.379, 0.159)$  | 1.248         | 99.01    |
| $(-0.4, 0.4)$   | $(-0.370, 0.318)$  | 1.480         | 99.15    |
| $(-0.4, 0.6)$   | $(-0.383, 0.532)$  | 1.751         | 99.06    |
| $(-0.4, 0.8)$   | $(-0.380, 0.700)$  | 1.949         | 99.04    |
| $(-0.6, 0.2)$   | $(-0.621, 0.172)$  | 1.219         | 99.08    |
| $(-0.6, 0.4)$   | $(-0.621, 0.342)$  | 1.399         | 99.01    |
| $(-0.6, 0.6)$   | $(-0.634, 0.594)$  | 1.587         | 98.96    |
| $(-0.6, 0.8)$   | $(-0.612, 0.761)$  | 1.704         | 98.82    |
| $(-0.8, 0.2)$   | $(-0.812, 0.187)$  | 1.194         | 98.97    |
| $(-0.8, 0.4)$   | $(-0.815, 0.360)$  | 1.321         | 99.20    |
| $(-0.8, 0.6)$   | $(-0.812, 0.580)$  | 1.416         | 98.64    |
| $(-0.8, 0.8)$   | $(-0.821, 0.801)$  | 1.418         | 98.99    |